

# Complex Faraday Rotation in Microstructured Magneto-optical Fiber Waveguides

Markus A. Schmidt, Lothar Wondraczek,\* Ho W. Lee, Nicolai Granzow, Ning Da, and Philip St. J. Russell

Magneto-optical glasses are of considerable current interest, primarily for applications in fiber circuitry, optical isolation, all-optical diodes, optical switching and modulation. While the benchmark materials are still crystalline, glasses offer a variety of unique advantages, such as very high rare-earth and heavy-metal solubility and, in principle, the possibility of being produced in fiber form. In comparison to conventional fiber-drawing processes, pressure-assisted melt-filling of microcapillaries or photonic crystal fibers with magneto-optical glasses offers an alternative route to creating complex waveguide architectures from unusual combinations of glasses. For instance, strongly diamagnetic tellurite or chalcogenide glasses with high refractive index can be combined with silica in an all-solid, microstructured waveguide. This promises the implementation of as-yet-unsuitable but strongly active glass candidates as fiber waveguides, for example in photonic crystal fibers.

Most current applications rely on MO crystals to provide large Verdet constants at acceptable levels of optical attenuation.<sup>[4]</sup> Today's benchmark material is yttrium-iron-garnet ( $\text{Y}_3\text{Fe}_5\text{O}_{12}$ ) (YIG).<sup>[5–7]</sup> It has high optical transparency throughout the visible and IR regions, provides a relatively large Verdet constant and can be processed using planar-etching and implantation techniques. On the other hand, planar optical isolators, per se, are limited to a relatively small number of applications due to geometric restrictions. However, although a fiber-optic approach is strongly desirable, it is difficult to implement because it relies on the availability of an MO glass<sup>[8]</sup> that is suitable for drawing into fiber.<sup>[9]</sup> As of now, MO glasses remain handicapped by a comparatively small Verdet constant,<sup>[10–12]</sup>

## 1. Introduction

Magneto-optical (MO) materials have found application in many areas of photonics, especially in the realization of optical isolators or diodes.<sup>[1]</sup> In such devices, optical isolation is achieved by altering the propagation of light by application of an external magnetic field. The magnetic field changes the optical response of the medium by inducing circular birefringence via the Faraday effect, resulting in a rotation of the plane of polarization of an incoming linearly polarized light beam.<sup>[2]</sup> The magnitude of the Faraday effect is governed by the Verdet constant,  $V_B$ , which is a characteristic property of the material. The macroscopic response is governed by the interaction of the magnetic field with microscopic magnetic moments that are inherent to the electronic structure of the material. Depending on the configuration of the electronic orbitals, MO materials can exhibit diamagnetic as well as paramagnetic responses, with the resulting Verdet constant often being larger or smaller than the sum of the individual contributions.<sup>[3]</sup>

although there has been significant progress in the design of novel magnetoactive glasses in recent years. Since the degree of Faraday rotation depends on the product of the Verdet constant and the optical path-length, materials with a smaller Verdet constant offer an attractive alternative to crystalline materials if the path-length can be increased and an MO glass can be identified, which is suitable for fiber, rod, or tube fabrication and stable against phase separation and crystallization, and produced in relatively large volumes of high purity and high homogeneity, also, ideally, being nontoxic. To fabricate an MO step-index fiber, the core material must have a refractive index that is higher than the cladding glass. Another approach is to use photonic crystal fibers (PCFs), which consist of an array of hollow channels parallel to the fiber axis.<sup>[13,14]</sup> As recently shown in fused silica PCF, these channels can be pressure-filled from the melt with many materials such as metals, semiconductors and low-melting-point glasses.<sup>[15–21]</sup>

The first step towards achieving a relatively large Verdet constant in a fiber was recently taken by drawing a step-index fiber from a heavily terbium-doped silica preform.<sup>[22–24]</sup> Such fiber-drawing processes, however, are limited to very specific combinations of core and cladding materials because their rheological and thermomechanical properties must be compatible. The PCF approach is an interesting alternative, offering more versatility in control of the guidance properties.

Here, we provide a review of recent progress in the development of MO glasses for waveguide applications. We present the first example of a hybrid MO waveguide, fabricated by pressure-assisted melt-filling of a fiber capillary. This points

Dr. M. A. Schmidt, H. W. Lee, N. Granzow, Prof. P. St. J. Russell  
Max Planck Institute for the Science of Light  
Guenther-Scharowsky Strasse 1, 91058 Erlangen, Germany  
Prof. L. Wondraczek, N. Da  
Department of Materials Science  
University of Erlangen-Nuremberg  
91058 Erlangen, Germany  
E-mail: lothar.wondraczek@ww.uni-erlangen.de

DOI: 10.1002/adma.201100364

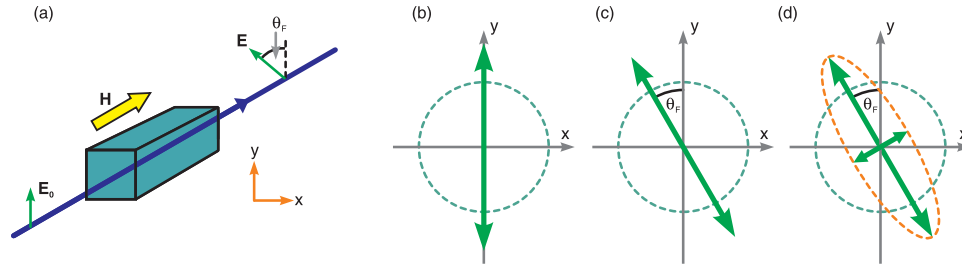


**Figure 1.** a) Propagation of a linear polarized beam through a longitudinally magnetized medium. a–c) Orientation and characteristics of the electric-field vector (green) at the output of the MO glass for three important scenarios. The coordinate system is a guide to the eye and the initial polarization is along the  $y$ -direction. b) Vanishing off-diagonal elements. c)  $\epsilon_{xy}$  is nonzero and real. The linear-input polarization state is rotated by the Faraday angle. d)  $\epsilon_{xy}$  is complex, leading to Faraday rotation and magnetic circular dichroism (MCD).

to the possibility of obtaining highly integrated MO architectures from unusual combinations of core and cladding glasses. We also discuss the consequences of the complex-valued off-diagonal matrix elements on the Faraday rotation.

## 2. The Faraday Effect and Magneto-optical Glasses

The physics behind the Faraday effect are illustrated in **Figure 1**. An external magnetic field causes the direction of linear polarization to rotate as light propagates through the MO medium. The light-matter interaction is governed by the dielectric matrix  $[\epsilon]$  of the material. When a static magnetic field is applied to an isotropic medium, pointing in the direction of propagation (taken to be along the  $z$ -axis), the dielectric tensor develops non-zero off-diagonal elements:

$$[\epsilon] = \begin{pmatrix} \epsilon_1 & -i\epsilon_{xy} & 0 \\ i\epsilon_{xy} & \epsilon_1 & 0 \\ 0 & 0 & \epsilon_3 \end{pmatrix}. \quad (1)$$

Note that under these conditions the Voigt effect, which appears when the  $B$ -field points perpendicular to the direction of propagation, is not present. Substituting this function into Maxwell's equations and assuming a plane-wave with harmonic time dependence  $(\vec{e}, \vec{h}) \exp[-i\omega t] \propto (\vec{E}, \vec{H}) \exp[i(\vec{\beta} \cdot \vec{r} - \omega t)]$ , the following master equation can be derived:

$$0 = \vec{\beta} (\vec{\beta} \cdot \vec{E}) - |\vec{\beta}|^2 \vec{E} + k_0^2 [\epsilon] : \vec{E} \quad (2)$$

where  $\vec{\beta} = \beta \hat{z}$  is the wavevector,  $k_0$  the vacuum wavevector and  $\vec{E}$  the electric-field vector. This equation can be rearranged as:

$$\begin{pmatrix} \epsilon_1 - n_z^2 & i\epsilon_{xy} & 0 \\ -i\epsilon_{xy} & \epsilon_1 - n_z^2 & 0 \\ 0 & 0 & \epsilon_3 \end{pmatrix} \begin{pmatrix} E_x \\ E_y \\ E_z \end{pmatrix} = 0, \quad (3)$$

where the refractive index in the  $z$ -direction is  $n_z = \beta/k_0$ . The third row of Equation 3 can be fulfilled only if  $E_z = 0$ , i.e., the

waves are transversely polarized, so that the matrix reduces to a  $2 \times 2$  system. When a magnetic field is applied in the  $z$ -direction, the off-diagonal elements cause coupling between the  $x$ - and  $y$ -electric-field components. An eigenmode analysis yields right (-) and left (+) circularly polarized solutions:  $\vec{E}_{\pm} = \hat{x}\vec{E}_{x\pm} \pm \hat{y}\vec{E}_{y\pm}$ , with eigenvalues  $n_{\pm}^2 = \epsilon_1 \pm \epsilon_{xy}$ . Since the Faraday effect is typically very small, the modal refractive indices can be approximated by  $n_{\pm} = n \pm \epsilon_{xy}/(2n)$  where  $n = \sqrt{\epsilon_1}$  is the refractive index of the medium. The resulting circular birefringence is  $\Delta n_z = n_+ - n_- \approx \epsilon_{xy}/n$ .

### 2.1. Faraday Rotation, the Verdet Constant and Magnetic Circular Dichroism (MCD)

In the case of a linear-input polarization state (e.g.,  $E_{x\pm}^0 = 1$ , **Figure 1a**), superposition of the two circularly polarized modes gives:

$$e_x(L) = (\vec{E}_{x+} \exp(in_+ k_0 L) + \vec{E}_{x-} \exp(in_- k_0 L))/2 \\ = e^{ink_0 L} \cos[\epsilon_{xy} k_0 L/n] \quad (4.1)$$

$$e_y(L) = (e^{ink_0 L} \sin(\epsilon_{xy} k_0 L/2) = e_x(L) \tan(\epsilon_{xy} k_0 L/2) \\ = e_x(L) \tan \theta_F \quad (4.2)$$

where  $\theta_F$  is the Faraday rotation. For linearly polarized input light and a real-valued  $\theta_F$ , the output polarization state is linear but rotated by  $\theta_F$ . The ability of the material to rotate the electric-field vector is characterized by the Verdet constant,  $V_B$ :

$$V_B = \theta_F / BL = \epsilon_{xy} \pi / (\lambda_0 n B) \quad (5)$$

where  $B$  is the magnetic-flux density. This expression neglects non-linear MO phenomena such as the Cotton-Mouton effect. Note that if  $\epsilon_{xy}$  is complex-valued,  $\theta_F$  is complex and circular dichroism  $\Delta\alpha_{CP}$  appears (**Figure 1b** and **c**). This is related to the difference in absorption coefficient between the left- and right-circularly polarized modes (**Figure 1d**):

$$\Delta\alpha_{CP} = 4\pi\epsilon_{xyi}/nk_0 = 4\theta_{Fi}/nL \quad (6)$$

Non-zero  $\Delta\alpha_{CP}$  causes the output polarization state to become elliptical, its principal axes being rotated relative to the linear-input polarization. The ellipticity (the ratio of field amplitudes

on the minor and major axes) is equal to the imaginary part of the Faraday rotation angle,  $\theta_{Fi}$ .

## 2.2. Non-reciprocal Wave Propagation and Optical Diodes

A well-known feature of magnetized media is the breakdown of time-reversal symmetry, linked to non-reciprocal propagation of light in the presence of a  $B$ -field pointing with (or against) the direction of propagation.<sup>[25,26]</sup> The operating principle of optical isolators (e.g., to prevent back reflection of undesired light into laser cavities) is based on such non-reciprocal behaviour.

## 2.3. MO Figure-of-Merit

A high-performance MO material should provide significant Faraday rotation within one optical-absorption length. A suitable figure-of-merit (FoM) can thus be defined as:

$$\text{FoM} = \frac{\theta_F}{\alpha BL} = \frac{V_B}{\alpha} \quad (7)$$

where  $\alpha$  is the exponential intensity-absorption rate.

## 2.4. Diamagnetic Glasses

Examples of diamagnetic species that can readily be incorporated into a glass network are  $\text{Pb}^{2+}$ ,  $\text{Sb}^{3+}$ ,  $\text{Te}^{4+}$ ,  $\text{Bi}^{3+}$  and  $\text{Tl}^+$ . In a diamagnetic glass it can be shown that the difference in refractive index experienced by two counter-rotating circularly polarized waves is given by:

$$\Delta n = n(\omega + \omega_L) - n(\omega - \omega_L) \approx \frac{e}{m} B \frac{dn}{d\omega} \quad (8)$$

where  $\omega_L = eB/2m$  is the Larmor frequency (electronic charge  $e$  and mass  $m$ ). This shows that optical dispersion of the MO material plays a key role in the magnitude of the Verdet constant:

$$V_B = \frac{e}{m} k_0 \frac{dn}{d\omega} \quad (9)$$

and that it is connected to the position of the electronic bandgap.<sup>[27,28]</sup> In a diamagnetic glass, large Verdet constants can only be obtained if the operating wavelength lies close to the band gap, where the optical dispersion is high. This also results in increased absorption and an unfavourably low FoM (Equation 7). The development of glasses with a high diamagnetic optical response is largely driven by the relatively low intrinsic temperature-dependence of the magnitude of the MO effect in these materials.<sup>[29]</sup> Typical systems are heavy-metal bismuthate glasses (e.g., cadmium, germanium and lead bismuthates<sup>[30]</sup>), tellurite glasses (tungsten, bismuth and lead tellurites<sup>[31]</sup>) and certain chalcogenides.<sup>[32]</sup>

## 2.5. Paramagnetic Glasses

If a diamagnetic glass is doped with paramagnetic ions such as  $\text{Tb}^{3+}$  or  $\text{Eu}^{3+}$ , a paramagnetic term must be included in the

analysis, resulting in an altered MO response. Paramagnetism arises from the non-zero angular momentum of the individual dopants ( $J \neq 0$ ), caused by the presence of unpaired electrons in the atomic orbitals.<sup>[33]</sup> The resulting magnetization  $M$  is then given by:<sup>[11]</sup>

$$M = Ng\mu_B J B_J(\xi) \quad (10)$$

where  $N$  is the number density of dopant atoms,  $g$  the Landé splitting factor,  $\mu_B$  the Bohr magneton,  $B_J$  the Brillouin function,  $J$  the total orbital quantum number, and where  $k_B$  is Boltzmann's constant and  $T$  is the temperature in Kelvin. At room temperature, the Brillouin function can be expanded in a Taylor series and the paramagnetic susceptibility approximated as:

$$\chi_p = \frac{NJ(J+1)g^2\mu_B^2}{3k_B T} \quad (11)$$

The effective Verdet constant can then be expressed as the sum of diamagnetic and paramagnetic contributions:

$$\begin{aligned} V_B &= V_B^{dia} + V_B^{par} = V_B^{dia} + A \frac{NJ(J+1)g^2\mu_B^2}{3k_B T} \\ &= V_B^{dia} + \frac{C}{T} \end{aligned} \quad (12)$$

with material constants  $A$  and  $C$  and  $V_B^{dia}$  given by Equation 9.  $C$  is generally negative, and hence the two contributions to the Verdet constant have opposite signs.

Paramagnetic ions suitable for incorporating into glasses are  $\text{Pr}^{3+}$ ,  $\text{Ce}^{3+}$ ,  $\text{Nd}^{3+}$ ,  $\text{Tb}^{3+}$ ,  $\text{Dy}^{3+}$  and  $\text{Eu}^{2+}$ , where  $\text{Eu}^{2+}$ <sup>[34]</sup> and  $\text{Tb}^{3+}$ <sup>[10,12,35–39]</sup> are currently receiving the greatest attention. As an alternative to rare-earth ions,  $\text{Fe}^{2+}$ -dopants are also being studied by some groups.<sup>[34,40]</sup> Most glass formers (matrix species) are diamagnetic, whereas paramagnetic behavior can normally only be obtained by heavy doping with rare-earth ions. To obtain a large MO response, a matrix with low diamagnetic  $V_B$  should be highly doped with strongly paramagnetic ions. Such glass designs, however, are limited by various secondary properties of the glass matrix, such as rare-earth solubility, kinetic fragility and liquidus temperature,<sup>[8]</sup> molar volume and refractive index, Abbé number and the position of the electronic resonances. From a qualitative point of view, successively higher MO performances may be expected from (in this order) vitreous silica, fluorophosphate, fluoride, borate, borosilicate, and aluminoboro (boro) silicate glasses (e.g., ref.<sup>[41–43]</sup>). As discussed later, some of these constraints may be overcome by using step-index fiber designs. As already mentioned, the Verdet constant resulting from doping with multiple rare-earth ions is not always a simple linear sum of the contributions of each ion, raising the possibility of very high values of  $V_B$ .<sup>[44]</sup> As a dopant species,  $\text{Tb}^{3+}$  offers the highest paramagnetic susceptibility ( $J = 6$  and  $g = 1.46$ ).<sup>[45]</sup> Hence, all commercially available MO glasses rely on massive  $\text{Tb}^{3+}$ -doping.<sup>[11,46,47]</sup>

Equation 11 shows that the magnetic susceptibility of paramagnetic glasses is inversely proportional to the temperature. As a result, above a critical temperature, only the diamagnetic contribution remains and  $V_B$  is given solely by  $V_B^{dia}$  (Equation 12).

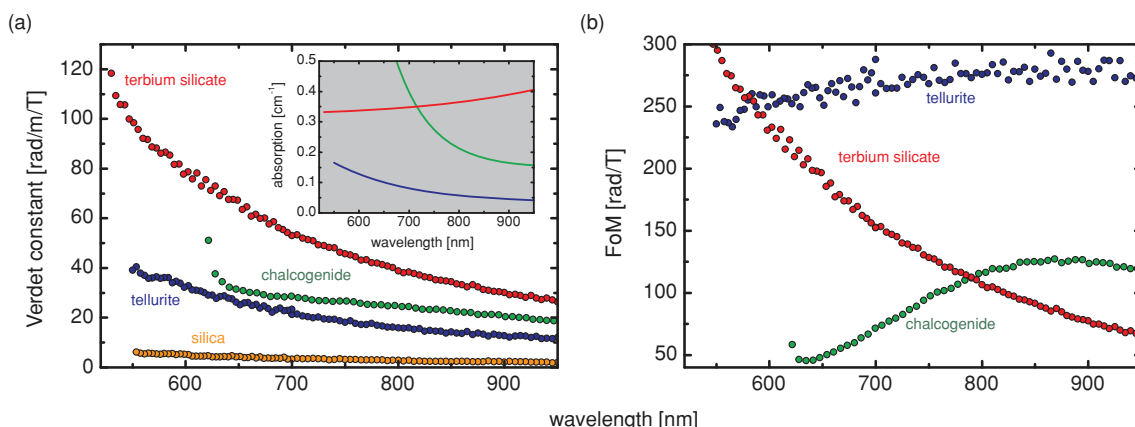


**Figure 2.** a) Wavelength dependence of the Verdet constant for different types of glasses (labels, described in text). The inset shows the absorption of chalcogenide (green), tellurite (blue) and terbium aluminosilicate (red) glass. b) The figure-of-merit, as calculated from Equation 7. Data were collected for various archetype glasses which were synthesized for the present report. Detailed information on specific glass properties may be obtained from, for example, ref.<sup>[11]</sup> and ref.<sup>[31,32]</sup>

## 2.6. Case Study I

We now explore complex Faraday rotation in several representative and application-relevant glass systems, initially focusing on bulk MO properties. In **Figure 2**, data for diamagnetic silica ( $\text{SiO}_2$ ), tellurite ( $77\text{TeO}_2\text{-}20\text{ZnO-}2.5\text{La}_2\text{O}_3$ ) and chalcogenide ( $\text{As}_2\text{S}_3$ ) glasses are summarized. As an example of a paramagnetic glass, terbium aluminosilicate ( $20\text{Tb}_2\text{O}_3\text{-}20\text{Al}_2\text{O}_3\text{-}30\text{SiO}_2\text{-}30\text{B}_2\text{O}_3$ ) was chosen. We were unable to detect any evidence of MO ellipticity (Figure 1) in any of these materials; that is to say, all of the off-diagonal elements of the dielectric tensor (Equation 1) are real-valued and there is no MCD. In diamagnetic glasses, the Verdet constant depends on the material dispersion via  $dn/d\omega$ . In all of the cases discussed here, the operating wavelength (vis-NIR) is on the low-frequency side of the electronic band gap, which is located at about 160 nm for the vitreous  $\text{SiO}_2$ ,<sup>[48]</sup> 350 nm for the terbium aluminosilicate, 400 nm for the tellurite glass and 580 nm for the chalcogenide glass.<sup>[49]</sup> As a result, the dispersion is normal ( $dn/d\omega < 0$ ) and the Verdet constant decreases at longer wavelengths (Figure 2a).

In the visible spectral range, vitreous silica has the flattest optical dispersion of all of the glasses studied and hence has an almost negligibly small Verdet constant (in accordance with Equation 9). On the other hand, a distinct increase of  $V_B$  can be observed at shorter wavelengths, especially in the case of the chalcogenides. At the same time, however, a trade-off arises between the closeness to the electronic resonance and the optical absorption or inelastic scattering. This trade-off is described by the MO FoM (Figure 2b). For example, even though the absolute value of  $V_B$  is higher for chalcogenide glasses, tellurite glasses appear more promising as real-world diamagnetic MO materials because of their higher FoM. Paramagnetic glasses, most prominently the Tb-aluminosilicate, on the other hand, typically achieve very large  $V_B$  ( $V_B > 80 \text{ rad mT}^{-1}$  for  $\lambda < 800 \text{ nm}$ ). Hence, they are studied in much-more detail for integration into fiber circuitry. Also in this case, however, optical absorption must be considered, and may result in a low FoM even for high  $V_B$ , especially in the near-IR, when

glasses are doped or contaminated with secondary species. The influence on the stoichiometry, that is to say, the contribution of the individual molecules to the magneto-optical activity, for one particular diamagnetic glass is shown in **Figure 3**. In short,  $\text{ZnO}$  and  $\text{La}_2\text{O}_3$  were added to the  $\text{TeO}_2$  matrix, primarily to stabilize the glass against crystallization and, thus enabling waveguide fabrication within a certain viscosity range. Reducing the  $\text{TeO}_2$  content from 77 mol% to 70 mol% leads to a reduction of  $V_B$  by about 10% throughout the entire measurement range. This clearly indicates that the  $\text{TeO}_2$  is responsible for the magneto-optical activity, i.e., the contributions from the  $\text{ZnO}$  and  $\text{La}_2\text{O}_3$  are negligible.

## 2.7. Case Study II

Here, we study a step-index fiber with an MO tellurite glass core and a fused silica cladding. Such a fiber (with high MO FoM)

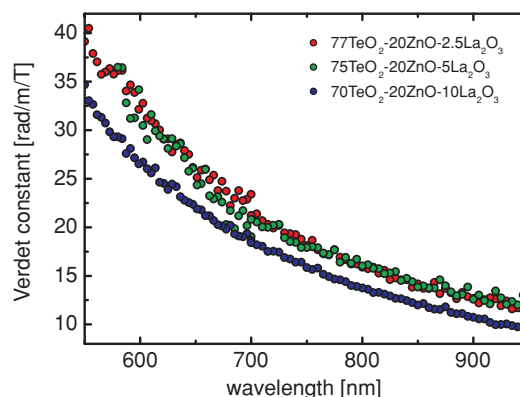


**Figure 3.** Wavelength dependence of the Verdet constant for different tellurite glasses. Red:  $77\text{TeO}_2\text{-}20\text{ZnO-}2.5\text{La}_2\text{O}_3$ , green:  $75\text{TeO}_2\text{-}20\text{ZnO-}5\text{La}_2\text{O}_3$ ; blue:  $70\text{TeO}_2\text{-}20\text{ZnO-}10\text{La}_2\text{O}_3$ . Further information on the MO activity of tellurite glasses may be obtained from, for example, ref. [11] and ref. [31].



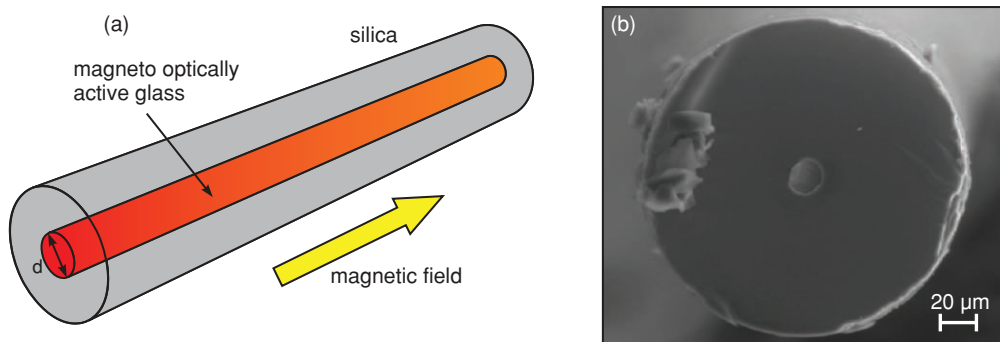


**Figure 4.** a) Sketch of magneto-optically active fiber waveguide, fabricated by using the pressure-assisted melt-infiltration technique. The yellow arrow indicates the direction of the externally applied magnetic field. b) Scanning-electron micrograph of the magneto-optically active waveguide investigated in the experiment (core diameter = 20  $\mu\text{m}$ , sample length = 8 cm, used core glass:  $77\text{TeO}_2\text{-}20.5\text{ZnO-}2.5\text{La}_2\text{O}_3$ ).

has potential as an all-glass optical isolator. Several attempts at creating MO fibers have been made, mostly relying on the use of heavily Tb-doped fiber-core materials and simultaneous drawing of, for example, rod-in-tube preforms.<sup>[22–24]</sup>

We have recently developed the technique of filling micro-capillaries or PCFs with low-melting-point glass by pressure-assisted melt infiltration (**Figure 4**).<sup>[16,17]</sup> This method involves pumping a low-viscosity material ( $<10\text{ Pa}\cdot\text{s}$ ) into the hollow channels. The required viscosity is obtained by heating to a suitable temperature, enabling filling with not only glasses but also, for example, metals or semiconductors.<sup>[15,16,18–20,50,51]</sup> If silica capillaries are used as the cladding material, the filling process is, theoretically, limited to a maximum temperature of about  $1200^\circ\text{C}$ . Hence, glass-forming materials must be chosen that have a sufficiently low melting temperature, such as chalcogenides,<sup>[16,17]</sup> tellurites<sup>[16,17]</sup> and phosphates.<sup>[52]</sup> In practice, we find that, at sufficiently small capillary diameters ( $<20\text{ }\mu\text{m}$ ), the core and cladding materials do not require matching coefficients of thermal expansion.<sup>[16,17]</sup> In the example in **Figure 4**, a silica capillary with an inner diameter of  $20\text{ }\mu\text{m}$  was filled with a diamagnetic tellurite glass ( $77\text{ TeO}_2\text{-}20.5\text{ ZnO-}2.5\text{ La}_2\text{O}_3$ ; SEM image in **Figure 4b**).<sup>[16,19]</sup> The polarization properties of a step-index fiber 8 cm long were measured under the influence of an external magnetic field (the wavelength dependence of  $V_B$  for the bulk glass is shown in **Figure 3**). In order to assess variations in the glass composition and structure that might have been caused by the filling process (selective evaporation, silica dissolution, etc.), the MO fibers were examined using scanning-electron microscopy and energy-dispersive X-ray spectroscopy (cross-section) and micro-Raman scattering (side-view, see **Figure 5**). Comparing the Raman spectra of the bulk and infiltrated glass reveals closely similar behaviors. No indication of confinement- or stress-induced short-range structural changes can be detected. The scattering peaks correspond to symmetric stretching and bending vibrations of Te-O-Te linkages between trigonal  $\text{TeO}_3$  pyramids,  $\text{TeO}_3^{+\delta}$  polyhedra and trigonal  $\text{TeO}_4$  bipyramids ( $\sim 420$  and  $477\text{ cm}^{-1}$ ), vibration of the continuous network of  $\text{TeO}_4$  bipyramids ( $\sim 611\text{ cm}^{-1}$ ), antisymmetric vibrations of Te-O-Te linkages ( $\sim 660\text{ cm}^{-1}$ ), stretching vibrations between tellurium and nonbridging oxygen sites ( $\sim 751\text{ cm}^{-1}$ ), and Te-O- stretching vibrations in  $\text{TeO}_3^{+\delta}$  polyhedra or  $\text{TeO}_3$  pyramids ( $\sim 805\text{ cm}^{-1}$ ).<sup>[53–56]</sup>

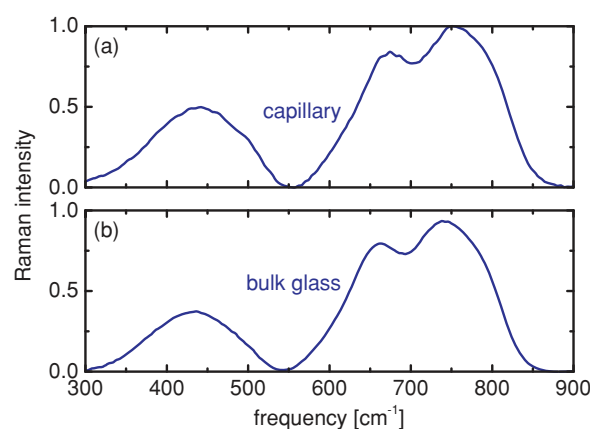


**Figure 5.** Comparison between micro-Raman spectra of filled-capillary and bulk tellurite glass ( $77\text{TeO}_2\text{-}20.5\text{ZnO-}2.5\text{La}_2\text{O}_3$ ): a) capillary (core diameter =  $20\text{ }\mu\text{m}$ ); b) bulk glass sample. See also ref. [16].

To study the MO response of the fiber and to compare it with bulk glass (which gives a much-stronger output signal), the monochromator was replaced with a narrow-band filter. Careful optical alignment is necessary to ensure that only the fundamental mode of the core is excited, since the waveguide core is relatively large and therefore is multimodal (number of modes in the visible range  $>1000$ ). Equation 5 was used to calculate the effective Verdet constant of the entire system, including any waveguide effects and the inherent material response (**Figure 6a**). It has to be pointed out that, due to the relatively large core diameter of  $20\text{ }\mu\text{m}$ , the penetration of the electromagnetic field into the silica cladding can be neglected (relative field concentration in the core  $>99.9\%$ ) and the polarization state of the core mode is purely linear. Both effects result in the fact that the pattern of the fundamental core mode has almost no influence on the calculated Verdet constant and we expect the light passing through the waveguide to behave like light passing through a bulk, MO-active glass. As in the case shown in **Figure 3**,  $V_B$  reduces for larger wavelengths. However, the magnitude of the effective Verdet constant is about half that of the bulk glass. This may be the consequence of morphological variations of the filled glass from its purely isotropic state, distortion of  $\text{TeO}_2$

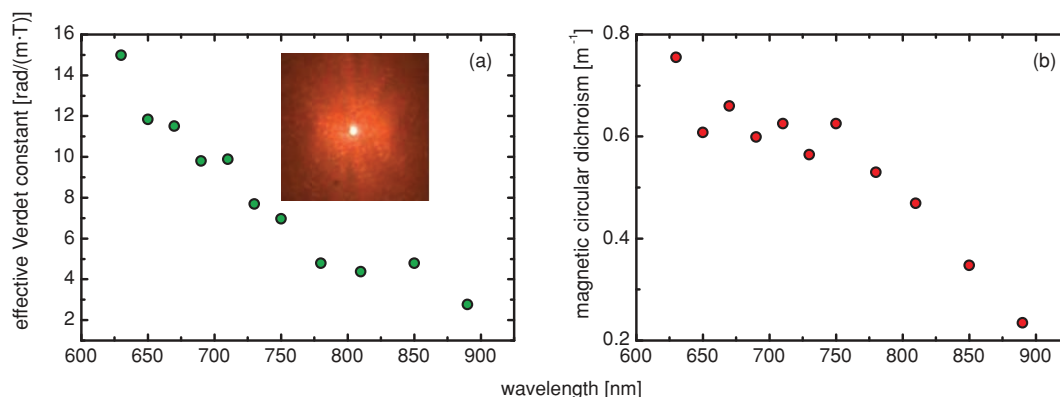


**Figure 6.** Characterization of the fundamental core mode of the magneto-optically active hybrid waveguide (core:  $77\text{TeO}_2\text{-}20.5\text{ZnO-}2.5\text{La}_2\text{O}_3$ , cladding: silica). Wavelength dependence of Verdet constant (a) and MCD (b). The inset in (a) shows the guided mode of the fiber when white light is launched into the input.

molecules, or a change in configuration number. While the latter two mechanisms have not yet been reported for tellurite melts, they would typically be expected at stress fields in the 100 MPa to GPa range (e.g., ref. [57,58]). In contrast to bulk (isotropic) glasses, distinct MCD could be observed in the fiber waveguides as a result of differing attenuation for right- and left-circularly polarized waves. As explained above, this means that the off-diagonal elements of the dielectric tensor are complex-valued, for reasons which are not yet completely clear, but may involve stress-related filling effects. Interestingly, beyond its implications for the performance of MO fiber waveguides, this observation suggests that the examination of polarization properties of such devices can be used to monitor pressure- and flow-induced structural changes of the filling medium.

### 3. Conclusions and Outlook

In summary, magneto-optical glasses are of interest for fiber-based optical isolators and circulators. While the benchmark materials are still crystalline, glasses offer a variety of unique advantages, such as compositional freedom, and, particularly, rare-earth and heavy-metal solubility. Although step-index MO fiber fabrication is, in principle, straightforward, it requires compatible combinations of viscosity-temperature dependence, crystallization stability and thermomechanical properties. Heavy doping of weakly diamagnetic glasses with paramagnetic species yields the highest Verdet constants, but they are often not suitable for applications because of: a) the strong temperature dependence of the paramagnetic response and b) the higher optical attenuation. Pressure-assisted filling of microcapillaries from the melt offers an alternative approach to fiber drawing. It permits the use of unusual glass combinations, for example, weakly diamagnetic silica with strongly diamagnetic tellurite glass. It may also be possible to incorporate heterogeneous media, such as nanocrystalline glass ceramics or low-melting-point glasses containing quantum dots, into MO fibers. The pressure-filling process also can be used to study stress-, flow- and confinement-induced structural variations in glass melts. It can also be used to fill photonic crystal

fibers with MO glasses, opening up further interesting device possibilities.

### 4. Methods

The MO data used in the present report were obtained for a series of archetype glasses (see text and Figure 2–3) which were prepared from analytical-grade raw materials in conventional melting and quenching experiments. The as-melted glasses were annealed stress-free at about 20 K above their respective glass-transition temperatures for 2 h and subsequently cooled to room temperature at a rate of 2 K  $\text{min}^{-1}$ . For characterization of the bulk MO characteristics, bars of square cross-section ( $80 \times 5 \times 5$  mm) were prepared from the as-annealed glasses. The capillary and PCF filling process is described in detail elsewhere.<sup>[16,17]</sup> In the experiments reported here, one end of the fiber capillary (inner diameter of 20  $\mu\text{m}$ ) was dipped into the tellurite melt at a viscosity of  $\sim 0.1$  Pa s, and a pressure-drop of 960 mbar was generated by applying a vacuum at the other end. During this process, the glass melt entered the capillary at a volume-filling rate of about  $10^{-12}$   $\text{m}^3 \text{s}^{-1}$  (filling speed: 10–100  $\text{mm min}^{-1}$ ).

To measure the MO properties, a set-up was constructed, consisting of a broadband (400 to 1600 nm) supercontinuum (SC) light source, a high-sensitivity polarimeter and a pulsed magnetic coil. The SC-light was collimated and passed through a wavelength-selective element (narrow-band-pass filter or monochromator) and a high-extinction-ratio polarizer to define a linear-input polarization state with an extinction ratio  $> 100\,000$  (Figure 2a). After passing through the sample (typical length 8 cm), the collimated light arrives at the polarimeter. In this way the incident polarization state is determined with an angular resolution of less than  $0.1^\circ$  and a minimum resolvable power of 0.1  $\mu\text{W}$ . To observe the Faraday effect, the sample was placed in an 8 cm long copper-wire coil (diameter = 1 mm, length = 200 m). Current pulses (20 ms in duration) of several amps created pulsed magnetic fields of up to 60 mT on the coil axis. The polarimeter was sufficiently fast to reach constant measurement values over the pulse length. Then, the differences of the polarization angle and the ellipticity between the on- and off-states were taken to calculate  $\theta_F$ .

The longitudinal field,  $B_z$ , along the central axis of the coil is given by:

$$B(z) = \frac{\mu_0 N I}{2 L_M} \left[ \frac{L_M/2 - z}{\sqrt{(L_M/2 - z)^2 + R^2}} + \frac{L_M/2 + z}{\sqrt{(L_M/2 + z)^2 + R^2}} \right] \quad (13)$$

where  $\mu_0$  is the magnetic susceptibility,  $I$  the current,  $N$  the number of windings, and  $L_M$  and  $R$  are the coil length and radius. The magnetic field was measured (using a Gauss meter) at points along the coil axis at constant current and the best fit to Equation 13 was found by adjusting the coil parameters. The optimum fit was obtained for  $N = 205$ ,  $R = 16.81$  mm and  $L_M = 36.9$  mm. The Faraday rotation angle was calculated by integrating Equation 13 over the sample length  $L$ . This gives rise to a geometrical factor,  $K_G$ , which is constant for a given sample and coil combination:

$$K_G(L_M, L) = \frac{(\sqrt{(L_M + L)^2 + 4R^2} - \sqrt{(L_M - L)^2 + 4R^2}) / 2L_M}{\quad} \quad (14)$$

and is plotted versus sample length in Figure 7b for the parameters of the coil used in the experiments.  $K_G$  approaches unity at large values of  $L$ , making the analysis very simple. However, the samples used in our experiments had lengths between 5 and 8 cm, requiring  $K_G$  to be included into the analysis. The Verdet constant is then given by:

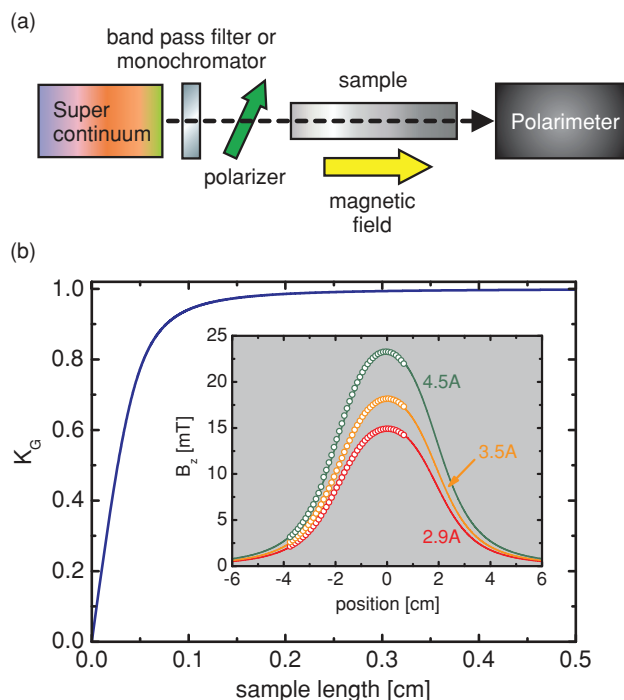


**Figure 7.** a) Experimental set-up to determine the complex Faraday rotation of bulk-glass samples or optical fibers. b) Geometrical factor  $K_G$  as function of sample length (calculated by Equation 14 and the parameters given in the text) Inset: Experimentally determined magnetic fields inside and outside the coil (points) together with the fits calculated by Equation 12 (lines). The different colors refer to different electrical currents through the coil (red: 2.9 A, orange: 3.5 A, green: 4.5 A).

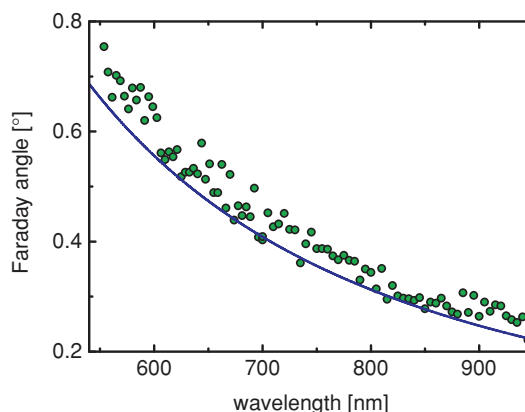


**Figure 8.** Faraday angle of a vitreous-silica glass sample. The green points refer to the experimentally determined values; the blue curve has been calculated using the parameters from ref. [28].

$$V_B = \frac{\theta_F}{\mu_0 N I K_G} \quad (15)$$

and the MCD can be calculated from Equation 6. Compared to conventional experiments, several important advantages arise from this approach. Only one polarizer is needed, which strongly simplifies the optical alignment. Orientation of the input polarizer is irrelevant, as the Faraday angle is a relative quantity between the on- and off- states. The setup is capable of detecting angle changes as small as  $0.1^\circ$ , limited only by the speed and the precision of the polarimeter itself. The Faraday angle, as well as the induced ellipticity, can be measured simultaneously, which allows determination of the complex off-diagonal elements, usually difficult to achieve in a polarizer-analyzer set-up. The set-up can easily be adapted to different sample geometries such as fiber waveguides and bulk glass samples – useful in the experiments reported here. No undesired sample-heating effects were observed, since the acquisition of one data point takes less than a second.

To test the set-up, the Verdet constant of fused silica in the visible spectral regime was measured and compared with values from the literature (Figure 8). Excellent agreement was obtained. Fused silica has one of the lowest Verdet constants of all glasses, demonstrating that the set-up can detect even very small Faraday rotations with high accuracy.

## Acknowledgements

This work was partly funded by the Deutsche Forschungsgemeinschaft (DFG) through the Cluster of Excellence “Engineering of Advanced Materials – EAM”. The capillary-filling experiments were supported by the DFG via grant no. WO1220/4-1.

Received: January 28, 2011  
Published online: April 12, 2011

- [1] A. K. Zvezdin, V. A. Kotov, *Modern Magneto-optics and Magneto-optical Materials*, Taylor & Francis Group, New York 1997.
- [2] J. M. Liu, *Photonic Devices*, Cambridge University Press, Cambridge 2005.

- [3] J. C. Suits, *IEEE Trans. Magn.* **1972**, 8, 95.
- [4] Lacklison, G. B. Scott, H. I. Ralph, J. L. Page, *IEEE Trans. Magn.* **1973**, 9, 457.
- [5] G. B. Scott, D. E. Lacklison, H. I. Ralph, J. L. Page, *Phys. Rev. B: Condens. Matter* **1975**, 12, 2562.
- [6] V. Doormann, J. P. Krumme, H. Lenz, *J. Appl. Phys.* **1990**, 68, 3544.
- [7] M. J. Weber, *Handbook of Optical Materials*, CRC Press, Boca Raton, FL **2002**.
- [8] N. F. Borrelli, *J. Chem. Phys.* **1964**, 41, 3289.
- [9] K. C. Kao, G. A. Hockham, P. I. Electr. Eng. **1966**, 113, 1151.
- [10] M. W. Shafer, J. C. Suits, *J. Am. Ceram. Soc.* **1966**, 49, 261.
- [11] a) A. B. Villaverde, E. C. C. Vasconcellos, *Appl. Opt.* **1982**, 21, 1347; b) J. A. Davis, R. M. Bunch, *Appl. Opt.* **1984**, 23, 633.
- [12] H. Y. Sui, Z. S. Xiao, *J. Appl. Phys.* **1994**, 75, 6375.
- [13] P. St. J. Russell, *Science* **2003**, 299, 358.
- [14] P. St. J. Russell, *J. Lightwave Technol.* **2006**, 24, 4729.
- [15] H. K. Tyagi, H. W. Lee, M. A. Schmidt, P. Uebel, N. Joly, M. Scharrer, P. St. J. Russell, *Opt. Lett.* **2010**, 35, 2573.
- [16] N. Da, L. Wondraczek, M. A. Schmidt, N. Granzow, P. St. J. Russell, *J. Non-Cryst. Solids* **2010**, 356, 1829.
- [17] M. A. Schmidt, N. Granzow, N. Da, M. Peng, L. Wondraczek, P. St. J. Russell, *Opt. Lett.* **2009**, 34, 1946.
- [18] H. K. Tyagi, M. A. Schmidt, L. P. Sempere, P. St. J. Russell, *Opt. Express* **2008**, 16, 17227.
- [19] M. A. Schmidt, L. N. Prill Sempere, H. K. Tyagi, C. G. Poulton, P. St. J. Russell, *Phys. Rev. B: Condens. Matter* **2008**, 77, 033417.
- [20] H. W. Lee, M. A. Schmidt, H. K. Tyagi, L. P. Sempere, P. St. J. Russell, *Appl. Phys. Lett.* **2008**, 93, 111102.
- [21] N. Da, A. A. Enany, N. Granzow, M. A. Schmidt, P. St. J. Russell, L. Wondraczek, *J. Non-Cryst. Solids* **2011**, 357, 1558.
- [22] L. Sun, S. Jiang, J. R. Marcianti, *Opt. Express* **2010**, 18, 12191.
- [23] L. Sun, S. Jiang, J. R. Marcianti, *Opt. Express* **2010**, 18, 5407.
- [24] L. Sun, S. B. Jiang, J. R. Marcianti, *IEEE Photonics Technol. Lett.* **2010**, 22, 999.
- [25] A. Yariv, *Optical Electronics in Modern Communications*, 5th ed, Oxford University Press, New York **1997**.
- [26] A. Yariv, P. Yeh, *Optical Waves in Crystals - Propagation and Control of Laser Radiation*, John Wiley & Sons, Inc., New York **1984**.
- [27] H. Sato, M. Kawase, M. Saito, *Appl. Opt.* **1985**, 24, 2300.
- [28] J. R. Qiu, K. Hirao, *J. Mater. Res.* **1998**, 13, 1358.
- [29] T. Kosuge, Y. Benino, V. Dimitrov, R. Sato, T. Komatsu, *J. Non-Cryst. Solids* **1998**, 242, 154.
- [30] C. B. Pedroso, E. Munin, A. B. Villaverde, N. Aranha, V. C. S. Reynoso, L. C. Barbosa, *J. Non-Cryst. Solids* **1998**, 231, 134.
- [31] N. V. Ovcharenko, T. V. Smirnova, *J. Non-Cryst. Solids* **2001**, 291, 121.
- [32] J. Qiu, J. B. Qiu, H. Higuchi, Y. Kawamoto, K. Hirao, *J. Appl. Phys.* **1996**, 80, 5297.
- [33] J. H. Van Vleck, M. H. Hebb, *Phys. Rev.* **1934**, 46, 46.
- [34] K. Tanaka, K. Fujita, N. Soga, J. R. Qiu, K. Hirao, *J. Appl. Phys.* **1997**, 82, 840.
- [35] J. Weber, *Proc. SPIE* **1986**, 681, 75.
- [36] S. Q. Xu, L. L. Hu, Z. H. Jiang, *J. Chin. Ceram. Soc.* **2003**, 31, 376.
- [37] H. R. Yin, C. X. Zhang, L. Y. Liu, B. J. Tang, *Mater. Rev.* **2008**, 22, 7.
- [38] J. Qiu, K. Maeda, R. Terai, H. Wakabayashi, *J. Non-Cryst. Solids* **1997**, 213, 363.
- [39] K. Tanaka, K. Hirao, N. Soga, *Jpn. J. Appl. Phys.* **1995**, 34, 4825.
- [40] H. Akamatsu, K. Fujita, S. Murai, K. Tanaka, *Appl. Phys. Lett.* **2008**, 92, 251908.
- [41] J. R. Qiu, K. Tanaka, N. Sugimoto, K. Hirao, *J. Non-Cryst. Solids* **1997**, 213, 193.
- [42] M. Daybell, W. C. Overton, H. L. Laguer, *Appl. Phys. Lett.* **1967**, 11, 79.
- [43] T. Hayakawa, K. Sato, K. Yamada, N. Kamata, N. Nishi, F. Maruyama, *Synth. Met.* **1997**, 91, 355.
- [44] T. Hayakawa, M. Nogami, N. Nishi, N. Sawanobori, *Chem. Mater.* **2002**, 14, 3223.
- [45] C. Kittel, *Introduction to Solid State Physics*, Wiley & Sons, New York **1995**.
- [46] H. G. Lee, Y. H. Won, G. S. Lee, *Appl. Phys. Lett.* **1996**, 68, 3072.
- [47] A. N. Malshakov, G. A. Pasmanik, A. K. Potemkin, *Appl. Opt.* **1997**, 36, 6403.
- [48] J. W. Fleming, *Appl. Opt.* **1984**, 23, 4486.
- [49] Y. L. Ruan, R. A. Jarvis, A. V. Rode, S. Madden, B. Luther-Davies, *Opt. Commun.* **2005**, 252, 39.
- [50] M. A. Schmidt, P. St. J. Russell, *Opt. Express* **2008**, 16, 13617.
- [51] C. G. Poulton, M. A. Schmidt, G. J. Pearce, G. Kakarantzas, P. St. J. Russell, *Opt. Lett.* **2007**, 32, 1647.
- [52] N. Da, S. Krolikowski, K. H. Nielsen, J. Kaschta, L. Wondraczek, *J. Am. Ceram. Soc.* **2010**, 93, 2171.
- [53] S. X. Shen, A. Jha, *Adv. Mater. Res.* **2008**, 39, 159.
- [54] V. G. Plotnichenko, V. O. Sokolov, V. V. Koltashev, E. M. Dianov, I. A. Grishin, M. E. Churbanov, *Opt. Lett.* **2005**, 30, 1156.
- [55] T. Sekiya, N. Mochida, A. Ohtsuka, M. Tonokawa, *J. Non-Cryst. Solids* **1992**, 144, 128.
- [56] H. Li, Y. Su, S. K. Sundaram, *J. Non-Cryst. Solids* **2001**, 293, 402.
- [57] L. Wondraczek, S. Sen, H. Behrens, R. E. Youngman, *Phys. Rev. B: Condens. Matter* **2007**, 76, 014202.
- [58] B. Mantis, S. Adichtchev, S. Sirotkin, L. Rafaely, L. Wondraczek, H. Behrens, C. Marcenat, N. V. Surovtsev, A. Pillonnet, E. Duval, B. Champagnon, A. Mermet, *J. Phys.: Condens. Matter* **2010**, 22, 025402.